

# A 3-mode, variable velocity jet model for HH 34

A. Raga<sup>1</sup> and A. Noriega-Crespo<sup>2</sup>

Received \_\_\_\_\_; accepted \_\_\_\_\_

arXiv:astro-ph/9808280v1 25 Aug 1998

---

<sup>1</sup>Instituto de Astronomía, UNAM, Ap. 70-264, 04510 México, D. F., México

<sup>2</sup>Infrared Processing and Analysis Center, CalTech-JPL, Pasadena, CA 91125, USA

## ABSTRACT

Variable ejection velocity jet models can qualitatively explain the appearance of successive working surfaces in Herbig-Haro (HH) jets. This paper presents an attempt to explore which features of the HH 34 jet can indeed be reproduced by such a model. From previously published data on this object, we find evidence for the existence of a 3-mode ejection velocity variability, and then explore the implications of such a variability. From simple, analytic considerations it is possible to show that the longer period modes produce a modulation on the shorter period modes, resulting in the formation of “trains” of multiple knots. The knots observed close to the source of HH 34 could correspond to such a structure. Finally, a numerical simulation with the ejection velocity variability deduced from the HH 34 data is computed. This numerical simulation shows a quite remarkable resemblance with the observed properties of the HH 34 jet.

*Subject headings:* Stars: Mass-loss — Hydrodynamics — Shock Waves — Star Formation — HH 34

## 1. Introduction

The Herbig-Haro (HH) object HH 34 presents a remarkable, jet-like structure that has been studied extensively over the years. The first extensive studies were carried out by Reipurth et al. (1986) and Bührke et al. (1988), presenting radial velocities, line ratios and images in different emission lines. Later work on this object includes high (Heathcote & Reipurth 1992) and low (Morse et al. 1993) resolution spectroscopy, Fabry-Perot imaging interferometry (Morse et al. 1992) and proper motion measurements (Eislöffel & Mundt 1992; Heathcote & Reipurth 1992).

There has also been a substantial amount of work in using deconvolutions to try to resolve the knots along the HH 34 jet (Raga & Mateo 1988; Bührke et al. 1988; Raga et al. 1991). These results have been superseded by the high resolution images of Reipurth & Heathcote (1992, who present images obtained with the ESO New Technology Telescope) and by the HST images (still not published in detail, but discussed in a partial way by Ray et al. 1996 and Reipurth et al. 1997). Unfortunately, these HST images have a rather low signal-to-noise ratio, complicating possible comparisons with theoretical models.

Recently, it has been shown that the HH 34 flow is the central part of a “superjet” (Bally & Devine 1994; Devine 1997; Eislöffel & Mundt 1997; Devine et al. 1997) extending over a total distance of  $\sim 3$  pc. This result puts the previous known facts of the HH 34 system in a totally new perspective. HH 34S (i. e., HH 34 itself, as listed in the catalog of Herbig 1974) has now been demoted from being the head of a jet, to being one of several “internal working surfaces” inside the blueshifted outflow lobe.

Finally, we should note that the source of HH 34 is visible optically. Rodríguez & Reipurth (1996) have detected a continuum VLA source that coincides (to within  $\sim 1''$ ) with the optically detected star. This is an important difference between HH 34 and the other well studied objects HH 46/47 and HH 111, which are seen to emerge from dense

cores which obscure the central source.

From the theoretical point of view, efforts have been made to compute 3/2-D bow shock models for reproducing images (Raga 1986) and line profiles (Morse et al. 1992) of HH 34S. Raga & Noriega-Crespo (1992) tried to apply such models for explaining the emission from the successive knots in the region between the source and 34S. This application of bow shock models to the aligned knots is based on the analytic work of Raga et al. (1990, see also Raga & Kofman 1992; Kofman & Raga 1992), who suggested that these knots could correspond to internal working surfaces resulting from an ejection velocity variability. This idea was pursued with 1D numerical simulations by Hartigan & Raymond (1993) and with cylindrically symmetric and 3D simulations by a number of authors (see, e. g., Stone & Norman 1993; Gouveia dal Pino & Benz 1994; Biro & Raga 1994; Smith et al. 1997b), and with high resolution simulations of single internal working surfaces (Falle & Raga 1993, 1995; Biro 1996). The interaction between successive working surfaces has also been studied. The statistical properties of the flow pattern resulting from many collisions between thin working surfaces were described by Raga (1992), and the shock reflection processes resulting from widening working surfaces (which get to touch each other) were described by Smith et al. (1997a).

The present paper discusses an application of models of jets from variable velocity sources to the case of the HH 34 jet. In particular, the region between the source and HH 34S itself is modeled, and no attempt is made to model the “superjet” beyond HH 34S (though the observations of this region are discussed in a partial way). The paper is organized as follows. Section 2 summarizes the results from analytic working surface models, and their implications for HH 34. Section 3 discusses previously obtained observational results for the knots along the HH 34 jet, and the derivation of the parameters of the source variability that can be carried out using the observations and the results from the

analytic models. Section 4 describes the results of a radiative, axisymmetric numerical simulation with the deduced parameters for the source variability. Finally, the results from this simulation are compared with observations of HH 34 in section 5.

## 2. Analytic working surface models

Let us now discuss some simple, analytic considerations that can be made about the formation and propagation of internal working surfaces. First, we derive simple expressions for the distances from the source at which working surfaces form, and at which they achieve maximum shock strengths (section 2.1). We then summarize some of the results of the asymptotic regime of large distances from the source (section 2.2). Finally, we discuss the qualitative features of jets from sources with multi-mode velocity variabilities (section 2.3). The qualitative implications of these results for the case of HH 34 are discussed.

### 2.1. The formation of internal working surfaces

Let us consider a jet from a source with a sinusoidal ejection velocity variability :

$$u_0(t) = v_0 + v_a \sin \omega_a t, \quad (1)$$

where  $v_0$  and  $v_a$  are constants, and  $\omega_a = 2\pi/\tau_a$  is the frequency of the variability (with  $\tau_a$  being the period). For the  $v_a \ll v_0$  case, from the results of Raga et al. (1990) it is straightforward to show that the working surfaces resulting from this ejection velocity variability are formed at a distance from the source :

$$x_c = \frac{v_0}{v_a} \frac{\Delta x}{2\pi}, \quad (2)$$

where

$$\Delta x = v_0 \tau_a, \quad (3)$$

is the separation between successive working surfaces. The velocity jump  $\Delta v$  across the working surface has a low (basically sonic) value close to the point in which the working surface is formed (i. e., at  $x = x_c$ ), and rapidly grows until it reaches a maximum  $\Delta v \approx 2v_a$  at a distance :

$$x_m \approx \frac{\pi}{2} x_c, \quad (4)$$

from the source.

These equations have direct implications for the formation of knots along HH jets. For the aligned knots radiating away from the sources of HH jets to be observable in optical atomic or ionic lines, they need to have shocks with velocities at least of order  $\sim 10 \text{ km s}^{-1}$ . From this, we conclude that we need to have  $v_a \approx 10 \text{ km s}^{-1}$  or larger. The velocities of HH jets indicate that  $v_0 \sim 100 \text{ km s}^{-1}$ . Inserting these values into equation (2), we conclude that the working surfaces have to form at a distance  $x_c \sim \Delta x$  from the source. Also, from equation (4) we see that the maximum shock strengths are also attained at a distance from the source which is comparable to the knot spacing. As we discuss in section 3, this general result does not appear to agree with the observed properties of the HH 34 jet.

## 2.2. The asymptotic regime of large distances from the source

In this section, we summarize some of the results of the asymptotic regime (of large distances from the source) studied by Kofman & Raga (1992) and Raga & Kofman (1992).

At large distances from the source (i. e., at distances several times larger than the knot separation  $\Delta x$ ), the velocity jump across the working surface is given by :

$$\Delta v = \frac{v_0^2 \tau_a}{x}, \quad (5)$$

where  $x$  is the distance from the source to the working surface, and  $v_0$  and  $\tau_a$  are defined in equation (1). Using a power law fit to the plane-parallel shock models of Hartigan et al. (1997), it is also possible to show that the  $H\alpha$  luminosity of the knots scales with distance as :

$$L_{H\alpha} \propto x^{-4.8}. \quad (6)$$

These results are used to interpret the observations of HH 34 in section 3.

### 2.3. Two-mode interactions

Finally, let us consider the more complex case of a two-mode ejection velocity variability :

$$u_0(t) = v_0 + v_s \sin \omega_s t + v_f \sin \omega_f t, \quad (7)$$

with a “slow” variability of amplitude  $v_s$  and period  $\tau_s = 2\pi/\omega_s$ , and a “fast” variability of amplitude  $v_f \ll v_s$  and period  $\tau_f = 2\pi/\omega_f \ll \tau_s$ .

The ejection velocity variability described by equation (7) is shown in Figure 1 for two sets of parameters. From this figure, it is clear that the values of the difference  $\Delta u_f$  between the minima and following maxima of the “fast” variability (see figure 1) are affected by the

presence of the “slow” variability. From an analysis of equation (7), it is straightforward to show that :

$$\begin{aligned} \Delta u_f(t) &= 2v_f \left\{ \sqrt{1 - \eta^2} + \eta \arcsin \left( \sqrt{1 - \eta^2} \right) \right\} ; \eta \leq 0 \\ \Delta u_f(t) &= 2v_f \left\{ \sqrt{1 - \eta^2} + \eta \left[ \pi - \arcsin \left( \sqrt{1 - \eta^2} \right) \right] \right\} ; \eta > 0, \end{aligned} \quad (8)$$

where the first branch of the arc sine is taken, and

$$\eta(t) = \eta_0 \cos \omega_s t, \quad \text{with } \eta_0 = \frac{v_s \tau_f}{v_f \tau_s}. \quad (9)$$

For  $|\eta| \ll 1$ , equation (8) takes the simple form :

$$\Delta u_f \approx 2v_f \left( 1 + \frac{\pi}{2} \eta \right). \quad (10)$$

From equation (8) or (10) it is possible to see that for  $\eta = 0$  (i. e., for a zero amplitude slow variability), we have  $\Delta v_f = 2v_f$ . During the time intervals in which the slow velocity variation is rising (i. e., when  $\eta > 0$ ), the velocity jumps associated with the fast variability are boosted upwards to values  $2v_f < \Delta u_f \leq 2\pi v_f$ . The maximum value of  $\Delta u_f = 2\pi v_f$  is attained for  $\eta = 1$  (see equation 8), and for  $\eta > 1$  the minima and maxima associated with the fast variability actually disappear (as illustrated in the second panel of figure 1). Conversely, for the time intervals with  $\eta < 0$  (see equation 9), we have values  $0 \leq \Delta u_f < 2v_f$ , with the lower value attained for  $\eta \leq -1$  (see equation 8).

From this discussion, we see that a long period variability of the source has the effect of “modulating” the shorter period variability. The short period, “fast mode” will produce working surfaces of increased strength for the time intervals in which the “slow mode”



variability gives a rising ejection velocity vs. time. Conversely, the “fast mode” produces working surfaces of decreased strength for the time intervals in which the “slow mode” gives a negative ramp of decreasing ejection velocity vs. time. This discussion strictly applies for two modes with parameters such that the condition  $\eta_0 < 1$  (see equation 9) is met.

In this way, the long period variability has the effect of modulating the knots along the jet (i. e., the working surfaces produced by the short period variability) into “trains” of knots of enhanced emission travelling down the jet beam. These trains of knots have a length of  $\sim v_s \tau_s / 2$ . The knots along the HH 34 jet could in principle correspond to such a train of knots resulting from the interaction of two modes of the ejection velocity variability.

### 3. Observations of HH 34

#### 3.1. HST images

We have reduced archival HST images of the HH 34 flow with the standard, pipeline reduction procedure. These images have been previously studied by Ray et al. (1996) and by Reipurth et al. (1997), but have not yet been analyzed completely.

The region from the source out to knot L is shown in Figure 2. From this figure we see that even though the region between the source and knot E (located at an angular distance of  $\approx 11''$  from the source) is very faint, the jet is still detected. The emission of this region appears to be somewhat narrower than the brighter region at distances larger than  $10''$  from the source (as pointed out by Ray et al. 1996).

An important question is why the region at distances  $< 10''$  from the source is so faint. A possible explanation of course is that the jet could be emerging from a high extinction region, which would extend out to a distance of  $\sim 10''$  from the source. The existence of such a high extinction region would also be a possible explanation for the lack

of an observable counterjet in the red-shifted lobe (out to the red-shifted working surface HH 34N, see, e. g., Bührke et al. 1988).

However, if the region close to the HH 34 source were subjected to high extinction, we would expect to see an apparent broadening of the jet beam towards the source, as a result of the existence of an increasingly strong scattered component. This broadening has been modeled (for the case of a jet emerging from a stratified clump) by Feldman & Raga (1991), who predict a quite dramatic spatial broadening of the emission as the observed intensity drops (as a result of increasing extinction and dispersion). The effect predicted by Feldman & Raga (1991) would be less dramatic for the case of a jet travelling within a cavity which has been opened up in the surrounding, stratified core.

The fact that in the HST images the jet emission becomes narrower at distances  $< 10''$  from the source (see above and Ray et al. 1996) therefore appears to rule out extinction as a possible explanation for the low intensity of this region. From this argument we then conclude that a model for the formation of knots in the HH 34 jet has to explain this sudden brightening of the jet at  $\approx 10''$  from the source. As is discussed below, this point is of particular interest.

For the HH 34 knots we have a spatial velocity  $v_0 \approx 200 \text{ km s}^{-1}$  (see section 3.2), an amplitude for the velocity variability of  $v_a \approx 20 \text{ km s}^{-1}$  (necessary to produce shocks which lead to observable emission), and a separation  $\Delta x \approx 2''$  between successive knots. Then, from equation (2) we obtain  $x_c \approx 3''$  and from equation (3)  $x_m \approx 5''$ . So, we would expect the knots along the jet to start brightening at  $\sim 3''$  away from the source, peak in intensity at  $\sim 5''$ , and decay for larger distances from the source. Therefore, we cannot explain the  $\sim 10''$  gap between the source and the bright knots along the HH 34 jet with a single-mode, sinusoidal source variability.

As we have described in section 2.3, two-mode interactions produce trains of knots

travelling down the jet beam. We tentatively identify the HH 34 knots with such a train. In the following, we explore in detail whether this interpretation is indeed appropriate for the knots along the HH 34 jet.

### 3.2. Proper motions, radial velocities and H $\alpha$ intensities

In order to evaluate the properties of the HH 34 jet in a more quantitative way, we now summarize the measurements that have been carried out of proper motions, radial velocities and H $\alpha$  fluxes for the knots along the jet. Figure 3 shows the spatial velocity and the luminosity of the knots as a function of distance from the source. The values shown in this figure are also tabulated in Table 1.

The distance from the source has been calculated assuming a distance to HH 34 of 450 pc, and an orientation angle  $\phi = 30^\circ$  between the axis of the outflow and the plane of the sky (there now seems to be a partial consensus on the value of this angle, see, e. g., Heathcote & Reipurth 1992; Morse et al. 1992; Raga et al. 1997a). The spatial velocity of the knots has been calculated by deprojecting the proper motion velocities measured by Heathcote & Reipurth (1992) (similar values are obtained by deprojecting the radial velocities), except for the knots HH 87, 88 (belonging to the S lobe of the HH 34 superjet), for which we have deprojected the radial velocities measured by Devine et al. (1997), as the proper motions measured for these knots appear to have larger errors.

We have computed the H $\alpha$  luminosities of the knots by integrating inside circular apertures with diameters chosen to include the emission of the successive knots, and then carrying out a background subtraction by using fields to the two sides of the outflow axis. For this calculation, we have used the HST archival H $\alpha$  image (for knots E through HH 34S), and the images of the superjet of Devine et al. (1997). A relative calibration between

the different images was obtained using the knots that appear in several images. Finally, the measured relative intensities were calibrated using the  $H\alpha$  flux measured for HH 34S by Morse et al. (1992).

From Figure 3 (also see table 1), we see that the spatial velocity of the knots initially rises (from knot E to knot G), then decays (from knot G to K) and finally rises monotonically (from knot O to HH 34S). The HH 87, 87 objects (belonging to the HH 34 superjet) show a substantially lower spatial velocity.

From this figure we also see that knots E-K and O have similar luminosities, and that HH 34S is by far the brighter condensation. On the  $H\alpha$  luminosity vs. position graph we have also plotted (with dashed lines, see figure 3) the  $L_{H\alpha} \propto x^{-4.8}$  law predicted from the asymptotic solution for large distances from the source (see equation 6). As pointed out by Raga & Kofman (1992), we see that knots I-L approximately fall on a single dashed line. However, all of the other knots fall on different lines.

This result implies the following. The observed knots are formed at a finite distance from the source (given by equation 2), rapidly reach their maximum intensity (at the distance given by equation 4), and then decay in intensity as they continue travelling away from the source with the predicted  $x^{-4.8}$  dependence. Looking at Figure 4, we then see that by the time that the knots E-L get to the present position of knot O, they will be fainter than the present knot O by more than 2 orders of magnitude. We therefore conclude that the variability giving rise to knots E-L is not the same variability as the one that gave rise to knot O. Analogously, we can argue that variabilities with different periods and amplitudes are also necessary for producing HH 34S and HH 87, 88.

In this way, we come up with a picture in which different modes of oscillation of the ejection velocity give rise to knots formed at different distances from the source. As these knots travel away from the source, they rapidly decay approximately following a  $x^{-4.8}$  law.

Given this rapid decay (and the existence of a detection limit in the observations), the positions of the observed knots have to be close (at least to an order of magnitude) to the position at which they were formed.

The observed distribution of knots therefore can be interpreted as evidence for the existence of different modes of oscillation of the ejection velocity. It is, however, not clear how to deduce the properties (period and amplitude) of these different modes. In the following two subsections we describe possible ways of deducing these properties for the knots of the outflow from the source out to HH 34S.

### 3.3. The HH 34S working surface

Let us now consider what ejection velocity variability is needed for producing the HH 34S working surface. Figure 4 is a schematic representation of the [S II] 6717+31 position-velocity diagram of HH 34S presented by Reipurth (1989a) and Heathcote & Reipurth (1992). From this figure, we see that the material feeding into the working surface from the upstream direction has a (de-projected) velocity  $v_1 = 344 \text{ km s}^{-1}$ , and that the working surface is overrunning downstream material which is propagating away from the source at a velocity  $v_2 = 214 \text{ km s}^{-1}$ . These two velocities straddle the value of the spatial velocity of HH 34S deduced from its proper motion (see table 1).

Using these velocities and the distance  $x_{34} = 8.0 \times 10^{17} \text{ cm}$  from the source to HH 34S, it is possible to compute the dynamical timescales

$$t_1 = \frac{x_{34}}{v_1} = 738 \text{ yr}, \quad (11)$$

$$t_2 = \frac{x_{34}}{v_2} = 1187 \text{ yr}, \quad (12)$$

of the material upstream and downstream of 34S (respectively). The material ejected between 738 and 1187 years ago (i. e., between  $t_1$  and  $t_2$ ) has been “processed” by the working surface (i. e., it has gone through one of the two working surface shocks, and has either piled up in the region between the two shocks or has been ejected sideways).

Let us assume that the HH 34S working surface is the result of a sinusoidal ejection velocity variability. From the values of  $v_1$  and  $v_2$  it is then possible to estimate the values of  $v_0$  and  $v_a$  (see equation 1) as :

$$v_0 \approx \frac{v_1 + v_2}{2} = 280 \text{ km s}^{-1}, \quad (13)$$

$$v_a \approx \frac{v_1 - v_2}{2} = 65 \text{ km s}^{-1}. \quad (14)$$

In order to obtain an estimate of the period of the variability, we consider the fact that HH 34S has to be at a distance from the source larger than the distance at which it is formed. In other words, we that  $x_{34} > x_c$ . From equations (2) and (3) we then have :

$$\tau_a < \frac{2\pi v_a}{v_0^2} x_{34} = 1425 \text{ yr}. \quad (15)$$

Also,  $\tau_a$  cannot be much smaller than this value, since we would otherwise already see a steep velocity rise along the jet as we go towards the source (corresponding to a “younger” working surface being formed by this variability). We therefore pick a value  $\tau_a = 1200 \text{ yr}$ . In this way, we have obtained estimates for the three parameters ( $v_0 = 280 \text{ km s}^{-1}$ ,

$v_a = 70 \text{ km s}^{-1}$  and  $\tau_a = 1200 \text{ yr}$ , see equation 1) of a hypothetical sinusoidal ejection velocity variability that gives rise to HH 34S.

### 3.4. The other knots

Let us first consider knots E-L. These knots are quasiperiodic, in the sense that the separation  $\Delta x$  between successive knots is quite constant. Using the knot positions and velocities tabulated in Table 1, we find a mean knot separation  $\langle \Delta x \rangle = 1.71 \times 10^{16} \text{ cm}$ , and a mean spatial velocity  $\langle v \rangle = 201 \text{ km s}^{-1}$ . From equation (3) we can then obtain the period  $\tau_b$  of the variability required to produce the observed knot structure :

$$\tau_b \approx \frac{\langle \Delta x \rangle}{\langle v \rangle} = 27.0 \text{ yr}. \quad (16)$$

Now, if we assume that the knots correspond to working surfaces in the asymptotic regime of large distances from the source, we can compute the velocity jump across the successive working surfaces through equation (5). Through this exercise we obtain velocity jumps in the  $\Delta v = 15\text{-}55 \text{ km s}^{-1}$  range.

If we assume that the ejection velocity variability producing these working surfaces is sinusoidal, it has to have a (half-)amplitude  $v_b$  of the order of  $\Delta v/2$ . So, we have to pick a value of  $v_b$  between 7 and 27  $\text{km s}^{-1}$ . For the numerical simulation described in the following section we have picked a  $v_b = 15 \text{ km s}^{-1}$  value.

Finally, we consider knot O. This knot is placed at a distance  $x_O = 4.2 \times 10^{17} \text{ cm}$  from the source (see table 1), and does not correspond to neither the variability mode of HH 34S nor the mode that forms knots E-I. We also see evidence for a third mode in the modulation of the flow velocity from knot E to L (see figure 3). A possible estimate for the period  $\tau_c$  of this third mode is :

$$\tau_c \approx 2 \frac{(x_O - x_G)}{(v_O + v_G)} = 310 \text{ yr}. \quad (17)$$

The amplitude  $v_c$  of this mode can be estimated as :

$$v_c \approx \frac{(v_G - v_K)}{2}, \quad (18)$$

(see figure 3). If we use the velocity values from Table 1 (which correspond to de-projected proper motions, see above), we obtain  $v_c \approx 50 \text{ km s}^{-1}$ . However, almost exactly one-half of this value is obtained evaluating (18) with the de-projected radial velocities of the knots. We therefore adopt a value  $v_c = 40 \text{ km s}^{-1}$  for the third mode of the ejection velocity variability.

#### 4. A numerical simulation

We now describe the results of a numerical simulation of a jet with a time-dependent ejection velocity given by :

$$u_0(t) = v_0 - v_a \sin \omega_a t + v_b \sin \omega_b t + v_c \sin \omega_c t, \quad (19)$$

with  $v_0 = 280 \text{ km s}^{-1}$ ,  $v_a = 70 \text{ km s}^{-1}$ ,  $\tau_a = 2\pi/\omega_a = 1200 \text{ yr}$  (see section 3.3),  $v_b = 15 \text{ km s}^{-1}$ ,  $\tau_b = 27 \text{ yr}$ ,  $v_c = 40 \text{ km s}^{-1}$  and  $\tau_c = 310 \text{ yr}$  (see section 3.4). We assume that the jet has a time-independent injection density (of atoms and ions)  $n_j = 500 \text{ cm}^{-3}$  and temperature  $T_j = 1000 \text{ K}$ , and that it travels into a uniform environment of density  $n_{env} = 5 \text{ cm}^{-3}$  and temperature  $T_{env} = 15 \text{ K}$ . Both the environment and the injected beam are assumed to be neutral, with the except of C and S which are assumed to be singly ionized. The jet has an initial radius  $r_j = 10^{16} \text{ cm}$ .



We should note that the initial radius that we have chosen for the jet is larger than the radius of the HH 34 jet by a factor of  $\sim 4$ . We have chosen such a larger radius in order to resolve the jet diameter with  $\sim 20$  points, which is already a quite limited resolution. Also, the initial density that we have chosen for the jet is too small probably by more than an order of magnitude. This choice is again forced on us by the limited spatial resolution of our numerical simulation (see below). With the lower density which has been chosen, we can marginally resolve the recombination regions behind the shocks in the flow, so that an approximate prediction of the emitted spectrum can be carried out.

The cylindrically symmetric gasdynamic equations, together with rate equations for up to six ions of H, He, C, N, O, Ne and S are integrated in time with the adaptive grid Coral code. A detailed description of this code, together with tests of the microphysical network, is given by Raga, Mellema and Lundqvist (1997), Raga et al. (1997b), and Mellema et al. (1998).

The cylindrical computational grid has an axial extent of  $10^{18}$  cm, a radial extent of  $2.5 \times 10^{17}$  cm, and has a 4-level binary adaptive grid with a maximum resolution of  $9.75 \times 10^{14}$  cm (in both the axial and radial directions). The jet is injected from the left side of the grid, and a reflection condition is applied on the  $x = 0$  plane for radii greater than  $r_j$ . In our simulation, the leading bow shock does not reach the outer radial boundary of the grid.

An outflow boundary condition is applied at the right hand side ( $x = 10^{18}$  cm) of the computational grid. In our simulation, the jet is allowed to propagate out of the computational grid, in order to simulate the fact that the HH 34 jet is preceded by previous ejection episodes (which form part of the “superjet”, see section 1).

In order to discuss the general characteristics of the flow, in Figures 5 and 6 we show the pressure stratification and on-axis cuts of the density, temperature and axial

velocity corresponding to time integrations of  $t = 1400$  and  $2900$  years, respectively. In the  $t = 1400$  yr frame (figure 5), the leading working surface of the jet is reaching the end of the computational grid. A series of working surfaces of different strengths can be seen :

- the leading working surface (at  $x \approx 10^{18}$  cm),
- two working surfaces with velocity jumps of  $\sim 100$  km s $^{-1}$  (at  $x \approx 6.5 \times 10^{17}$  cm and  $x \approx 7.5 \times 10^{17}$  cm),
- a number of “small” working surfaces (with velocity jumps of  $\sim 20$ - $50$  km s $^{-1}$ ) close to the injection point (with  $x < 10^{17}$  cm).

As is clear from the axial velocity cut (bottom panel of figure 5), the velocity jumps across the “small” working surfaces rapidly decay and disappear for distances  $x > 10^{17}$  cm. However, these working surfaces still can be seen at larger distances from the source as clumps of enhanced density and temperature which cool as they travel away from the source.

The two working surfaces at  $x \sim 10^{17}$  cm move at different velocities ( $v_x \approx 320$  km s $^{-1}$  for the  $x \approx 6.5 \times 10^{17}$  cm working surface, and  $v_x \approx 250$  km s $^{-1}$  for the  $x \approx 7.5 \times 10^{17}$  cm working surface). Because of this difference in their velocities, the two working surfaces merge into a single shock structure before getting to the end of the computational grid. Such working surface mergers are characteristic of multi-mode variable ejection velocity models.

In Figure 6, we show the flow stratification corresponding to a  $t = 2900$  yr time integration. The leading working surface of the flow has of course left the computational grid by now. However, the far wings of the leading bow shock can still be seen as an outwardly propagating, almost cylindrical shock wave (located at a radius  $r \approx 1.5 \times 10^{17}$  cm,

see the top panel of figure 6). Otherwise, the flow stratification is qualitatively similar to the one found for the  $t = 1400$  yr time integration (see figure 6).

We judge that the evolution close to the  $t = 2900$  yr time frame is more appropriate for carrying out comparisons with the HH 34 jet, since in the observations we have clear evidence (see section 1) that HH 34S is not the leading working surface of the outflow. In the following section we then discuss the time-sequence of the flow around  $t \sim 3000$  yr on the basis of the predicted intensity maps.

## 5. Comparisons between theory and observations

In order to deduce the parameters for the ejection velocity variability of our model, we have used the radial velocities, proper motions and knot positions observed for the HH 34 jet. Therefore, by construction our numerical model has knots with positions and kinematical properties which agree well with the observations of HH 34.

However, for the determination of the model parameters we have not used the observed line intensities. It is therefore of interest to compute intensity maps from our numerical simulation, and to compare them with images of HH 34. This comparison to some extent is an independent check on the applicability of a variable ejection velocity model for this object.

Figure 7 shows a time sequence of  $H\alpha$  intensity maps computed from the numerical simulation described in section 4. The maps have been computed at intervals of  $\Delta t = 100$  yr, starting at an integration time  $t_0 = 2500$  yr. An angle of  $30^\circ$  (as appropriate for HH 34, see section 3) between the outflow axis and the plane of the sky has been assumed, and the maps have not been convolved with a simulated point spread function. As is clear from Figure 7, our model produces images which are qualitatively similar to several jet-like HH

objects , e. g., HH 111 (Reipurth 1989b; Reipurth et al. 1997) and HH 228 (the outflow associated with Th 28, see Krautter 1986; Graham & Heyer 1989).

In our model, the short period, low amplitude knots are modulated into “trains” of knots by the intermediate period variability. Also, the successive trains of knots have different intensities as a result of the modulation by the long period variability mode. As a result of this 3-mode interaction, quite different morphologies are obtained as the time integration progresses, and the relative phases of the three modes change.

From the time sequence of Figure 7, we choose the  $t = 2900$  yr frame. In Figure 8, we show a comparison of the predicted  $H\alpha$  and  $[S II] 6717+6731$  maps for this time frame with the corresponding observations of the HH 34 jet. From this comparison, it is clear that our numerical model produces intensity maps which are qualitatively quite similar to the ones of HH 34.

In order to quantify this result, in Figure 9 we have plotted the observed and predicted  $H\alpha$  luminosities of the consecutive knots as a function of de-projected distance from the source. The most important difference between the predictions and the observations is that the predicted luminosities are lower than the observed ones by a factor of  $\sim 100$ . This result indicates that the initial number density that we chose for the jet in our simulation ( $n_j = 500 \text{ cm}^{-3}$ , see section 4) is probably too low by a factor of  $\sim 100$  with respect to the initial density of the HH 34 jet.

If we multiply the predicted luminosities by a factor of 100 (see figure 9), we find that the predictions match the observed luminosities of the successive knots along the HH 34 jet to within a factor of  $\sim 10$ . Given the extremely strong dependence of the predicted luminosities on shock velocity (see, e. g., Hartigan, Raymond and Hartmann 1987; Raga & Kofman 1992), this agreement is nothing short of surprising.

With the initial jet density ( $n_j \approx 5 \times 10^4 \text{ cm}^{-3}$ ) necessary to reproduce the observed luminosities, and the initial jet radius  $r_j = 10^{16} \text{ cm}$  and average velocity  $v_0 = 280 \text{ km s}^{-1}$  of our simulated jet (see section 4), we can compute an average mass loss rate of  $\dot{M} \approx 1.6 \times 10^{-5} \text{ M}_\odot \text{ yr}^{-1}$  for the HH 34 jet.

It would of course be interesting to carry out a comparison between, e. g., the predicted morphologies and line ratios for the successive knots and the corresponding observations. However, our numerical simulation does not have a high enough spatial resolution for such comparisons to be meaningful.

## 6. Conclusions

We have first reviewed the analytic models for the formation and propagation of internal working surfaces, and derived a simple analytic description of the interaction between different oscillation modes of the ejection velocity variability. We find that multi-mode ejection velocity variabilities lead to the formation of “trains” of knots travelling away from the source.

Using these analytic models, we have proceeded to analyze the observations of the HH 34 jet which have been obtained in the past. Through this analysis, we have derived three modes for an assumed ejection velocity variability of the source of HH 34.

These modes have periods and (half-)amplitudes :

- $\tau_a = 1200 \text{ yr}, v_a = 70 \text{ km s}^{-1}$ ,
- $\tau_b = 27 \text{ yr}, v_b = 15 \text{ km s}^{-1}$ ,
- $\tau_c = 310 \text{ yr}, v_c = 40 \text{ km s}^{-1}$ ,

and a  $v_0 = 280 \text{ km s}^{-1}$  average velocity. If we plot these periods and amplitudes logarithmically, it is clear that they closely follow a  $v \propto \tau^{0.4}$  power law (see figure 10). Due to the uncertainties in the determination of these parameters, however, this result should probably be taken as a mere curiosity.

We have then proceeded to carry out a numerical simulation of a jet with this ejection velocity variability. From this simulation, we obtain predicted H $\alpha$  (and [S II] 6717+6731) intensity maps which are qualitatively very similar to the corresponding observations of the HH 34 jet. In order to reproduce the luminosities of the observed knots, we find that we would need an initial number density for the jet which is 2 orders of magnitude larger than the one we have used. However, with the resolution of our simulation, we cannot use such a high density (as the cooling regions would then be completely unresolved).

From our model fit to the HH 34 jet, we obtain an estimate of  $\dot{M} \approx 1.6 \times 10^{-5} \text{ M}_{\odot} \text{ yr}^{-1}$  for this outflow. Interestingly, this estimate is about an order of magnitude larger than the mass loss rate computed by Raga (1991) on the basis of a comparison with a steady jet model, and about three orders of magnitude higher than the less elaborate estimate of Mundt, Brugel and Bührke (1987). These differences are a good illustration of the fact that mass loss rate estimates for HH jets are very highly model dependent.

The work of A. Raga was supported by grants from DGAPA, CONACyT and the UNAM/Cray program. We would like to thank Bo Reipurth and Steve Heathcote for providing us with their ESO NTT images of HH 34. Also, we would like to thank Dave Devine, Bo Reipurth and John Bally for providing us with their images of the HH 34 superjet.

## REFERENCES

- Bally, J., & Devine, D. 1994, ApJ, 428, L65.
- Biro, S. 1996, MNRAS, 278, 990.
- Biro, S., & Raga, A. C. 1994, ApJ, 434, 221.
- Bührke, T., Mundt, R., & Ray, T. P. 1988, A&A, 200, 99.
- Devine, D. 1997, in *Low Mass Star Formation, from Infall to Outflow*, poster proc. of IAU Symp. 192, eds. F. Malbet & A. Castets (Grenoble : Obs. de Grenoble), p. 95.
- Devine, D., Bally, J., Reipurth, B., & Heathcote, S. 1997, AJ, 114, 2095.
- Eislöffel, J., & Mundt, R. 1992, A&A, 263, 292.
- Eislöffel, J., & Mundt, R. 1997, AJ, 114, 280.
- Falle, S. A. E. G., & Raga, A. C. 1993, MNRAS, 261, 573.
- Falle, S. A. E. G., & Raga, A. C. 1995, MNRAS, 272, 785.
- Feldman, H., & Raga, A. C. 1991, AJ, 102, 2049.
- Gouveia dal Pino, E., & Benz, W. 1994, ApJ, 435, 261.
- Graham, J. A., & Heyer, M. H. 1988, PASP, 100, 1529.
- Hartigan, P., & Raymond, J. C. 1993, ApJ, 409, 705.
- Hartigan, P., Raymond, J. C., & Hartmann, L. 1987, ApJ, 316, 323.
- Heathcote, S., & Reipurth, B. 1992, AJ, 104, 2193.
- Herbig, G. H. 1974, Lick Obs. Bull., No. 658.

- Kofman, L., & Raga, A. C. 1992, *ApJ*, 390, 359.
- Krautter, J. 1986, *A&A*, 161, 195.
- Mellema, G., Raga, A. C., Cantó, J., Lundqvist, P., Balick, B., Steffen, W., & Noriega-Crespo, A. 1998, *A&A*, 331, 335.
- Morse, J. A., Hartigan, P., Cecil, G., Raymond, J. C., & Heathcote, S. 1992, *ApJ*, 399, 231.
- Morse, J. A., Heathcote, S., Hartigan, P., & Cecil, G. 1993, *AJ*, 106, 1139.
- Mundt, R., Brugel, E. W., & Bührke, T. 1987, *ApJ*, 319, 275.
- Raga, A. C., 1986, *AJ*, 92, 637.
- Raga, A. C., 1991, *AJ*, 101, 1472.
- Raga, A. C., 1992, *MNRAS*, 258, 301.
- Raga, A. C., & Binette, L., 1991, *RMxAA*, 22, 265.
- Raga, A. C., Cantó, J., Binette, L., & Calvet, N. 1990, *ApJ*, 364, 601.
- Raga, A. C., Cantó, J., Curiel, S., Noriega-Crespo, A., & Raymond, J. C. 1997a, *RMxAA*, 33, 157.
- Raga, A. C., Noriega-Crespo, A., Cantó, J., Steffen, W., Van Buren, D., Mellema, G., & Lundqvist, P. 1997, *RMxAA*, 33, 73.
- Raga, A. C., Mellema, G., & Lundqvist, P. 1997, *ApJS*, 109, 517.
- Raga, A. C., & Kofman, L. 1992, *ApJ*, 386, 222.
- Raga, A. C., & Mateo, M. 1988, *AJ*, 95, 543.
- Raga, A. C., & Noriega-Crespo, A. 1992, *RMxAA*, 24, 9.



Raga, A. C., Mundt, R., & Ray, T. P. 1991, *A&A*, 252, 733.

Ray, T. P., Mundt, R., Dyson, J. E., Falle, S. A. E. G., & Raga, A. C. 1996, *ApJ*, 468, L103.

Reipurth, B. 1989a, in *Low Mass Star Formation and Pre-Main Sequence Objects*  
(Garching : ESO), p. 247.

Reipurth, B. 1989b, *Nature*, 340, 42.

Reipurth, B., Bally, J., Graham, J. A., Lane, A. P., & Zealy, W. G. 1986, *A&A*, 164, 51.

Reipurth, B., Hartigan, P., Heathcote, S., Morse, J. A., & Bally, J. 1997, *AJ*, 114, 757.

Smith, M. D., Suttner, G., & Zinnecker, H. 1997, *A&A*, 320, 325.

Smith, M. D., Suttner, G., & Yorke, H. W. 1997, *A&A*, 323, 223.

Stone, J., & Norman, M. L. 1993, *ApJ*, 413, 198.

Table 1. Parameters of the knots along the HH 34 jet

Knot	$x^1(\text{cm})$	$L(L_\odot)$	$v^2(\text{km s}^{-1})$
E	$9.64 \times 10^{16}$	$1.46 \times 10^{-5}$	201
F	$1.12 \times 10^{17}$	$1.10 \times 10^{-5}$	256
G	$1.31 \times 10^{17}$	$1.09 \times 10^{-5}$	288
I	$1.50 \times 10^{17}$	$2.08 \times 10^{-5}$	209
J	$1.63 \times 10^{17}$	$1.32 \times 10^{-5}$	209
K	$1.84 \times 10^{17}$	$7.82 \times 10^{-6}$	184
L	$2.16 \times 10^{17}$	$2.34 \times 10^{-6}$	240
O	$4.20 \times 10^{17}$	$1.42 \times 10^{-5}$	318
34S	$8.01 \times 10^{17}$	$2.26 \times 10^{-3}$	329
87	$5.14 \times 10^{18}$	$9.24 \times 10^{-4}$	80
88	$5.38 \times 10^{18}$	$3.08 \times 10^{-4}$	50

<sup>1</sup>de-projected distances from the source to knot center

<sup>2</sup>de-projected proper motion velocities, except for knots 87,88 for which de-projected radial velocities are given

Fig. 1.— Diagram showing the time-dependent ejection velocity  $u_0(t)$  for two-mode variabilities. The graphs show the results for two different combinations of parameters (listed below each panel), which are discussed in the text.

Fig. 2.—  $H\alpha$  and [S II] 6717+6731 HST images of the region close to the source of HH 34. The images are shown with a logarithmic greyscale (covering different ranges for each of the images, as shown by the wedges to the right of the panels). The region within  $10''$  of the source shows a number of very faint and narrow knots, which are seen more distinctly in the [S II] image.

Fig. 3.— Spatial velocities (top) and  $H\alpha$  luminosities (bottom) as a function of the de-projected distance  $x$  from the source of HH 34. The dashed lines in the bottom panel show the  $L_{H\alpha} \propto x^{-4.8}$  evolution predicted for the knots from the asymptotic solution for large distances from the source. The  $H\alpha$  luminosities have been obtained from measurements on images kindly provided to us by Heathcote, Reipurth, Devine and Bally.

Fig. 4.— Schematic representation of the position-velocity diagram of HH 34S of Heathcote & Reipurth (1992). The slit was aligned with the outflow axis, and the direction away from the outflow source is towards the right. The velocity of the surrounding cloud is shown with a solid, horizontal line. The working surface is seen to be overrunning weakly emitting material with a (de-projected) velocity  $v_2 = 214 \text{ km s}^{-1}$ . The jet is feeding into the working surface from the upstream direction with a (de-projected) velocity  $v_1 = 344 \text{ km s}^{-1}$ .

Fig. 5.— Flow stratification obtained from the numerical simulation described in the text for a  $t = 1400 \text{ yr}$  time integration. The top panel shows the pressure stratification of the flow (with factor of 2 contours). The three bottom panels show number density (of atoms and ions), temperature and axial velocity cuts down the symmetry axis of the flow.

Fig. 6.— Flow stratification obtained from the numerical simulation described in the text

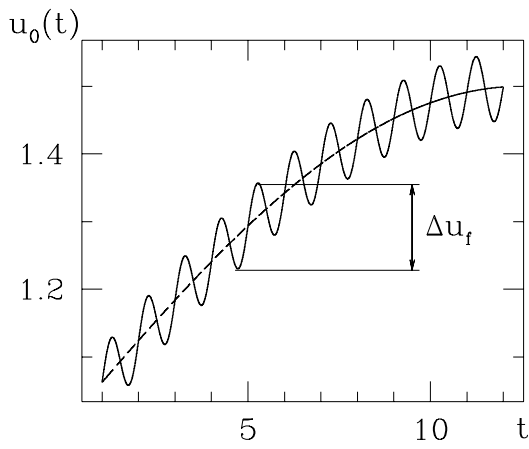
for a  $t = 2900$  yr time integration. The top panel shows the pressure stratification of the flow (with factor of 2 contours). The three bottom panels show number density (of atoms and ions), temperature and axial velocity cuts down the symmetry axis of the flow.

Fig. 7.— Logarithmic greyscale representation of the  $H\alpha$  intensity maps predicted from the numerical simulation described in the text for time integrations  $t = 2500$  (top panel), 2600, 2700, 2800, 2900 and 3000 yr (bottom panel). The maps have been normalized so that the peak intensity in the leading working surface of the  $t = 2900$  yr panel has a value of 1.

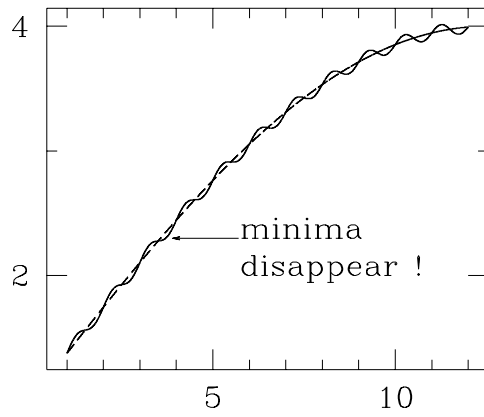
Fig. 8.— Comparison of the  $H\alpha$  and [S II] 6717+6731 images predicted from the numerical simulation described in the text for a  $t = 2900$  yr time integration and images of the HH 34 outflow in the corresponding lines. The images have been scaled arbitrarily, and a constant background has been subtracted from the observations. The colours represent a logarithmic scale, covering the same range for the predicted and the corresponding observed images. A smaller range has been used for the  $H\alpha$  images, since the observed  $H\alpha$  image has a smaller dynamic range (see the wedges on the right-hand side of the plots). The predicted images have the same spatial coverage as the frames of Figure 7. The HH 34 images have been scaled in an approximate way, assuming a distance of 450 pc. The observations of HH 34 have been previously published by Heathcote & Reipurth (1992), who we thank for kindly having provided us with the images.

Fig. 9.—  $H\alpha$  luminosities of the knots along HH 34 (squares) as a function of de-projected distance from the source (also see table 1). The luminosities predicted for the knots seen in the  $t = 2900$  yr  $H\alpha$  image from the numerical simulations are plotted (after having been multiplied by a factor of 100) as crosses.

Fig. 10.— Logarithmic plot of the velocity half-amplitude of the three modes (used to model HH 34) as a function of their period. The straight line corresponds to a  $v \propto v^{0.4}$  power law.

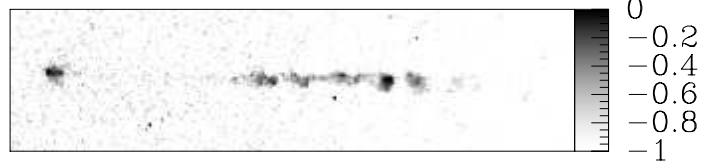


$v_0=1$   
 $v_f=0.05, \tau_f=1$   
 $v_s=0.5, \tau_s=50$



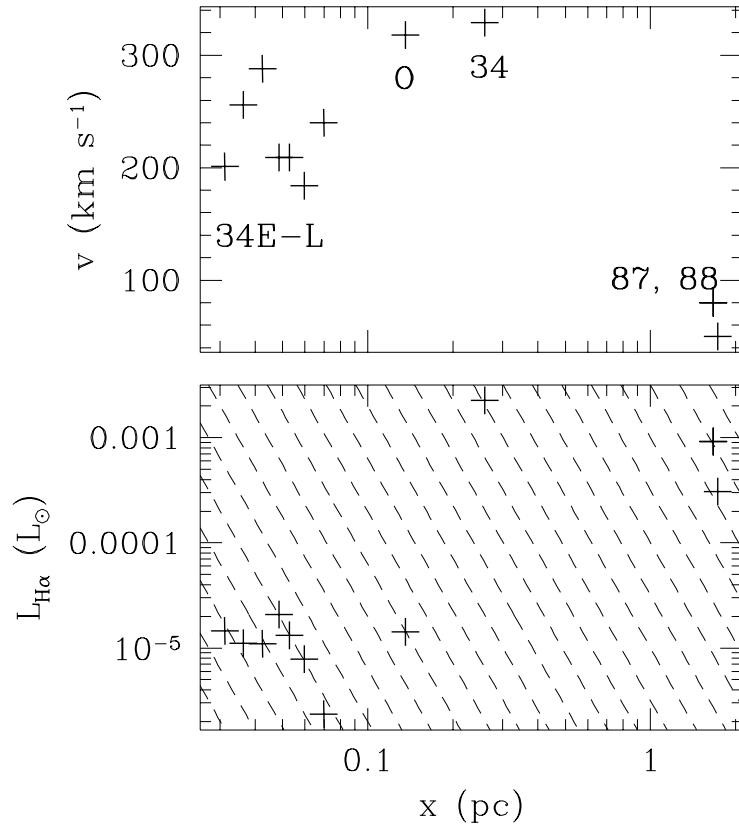
$v_0=1$   
 $v_f=0.05, \tau_f=1$   
 $v_s=3, \tau_s=50$

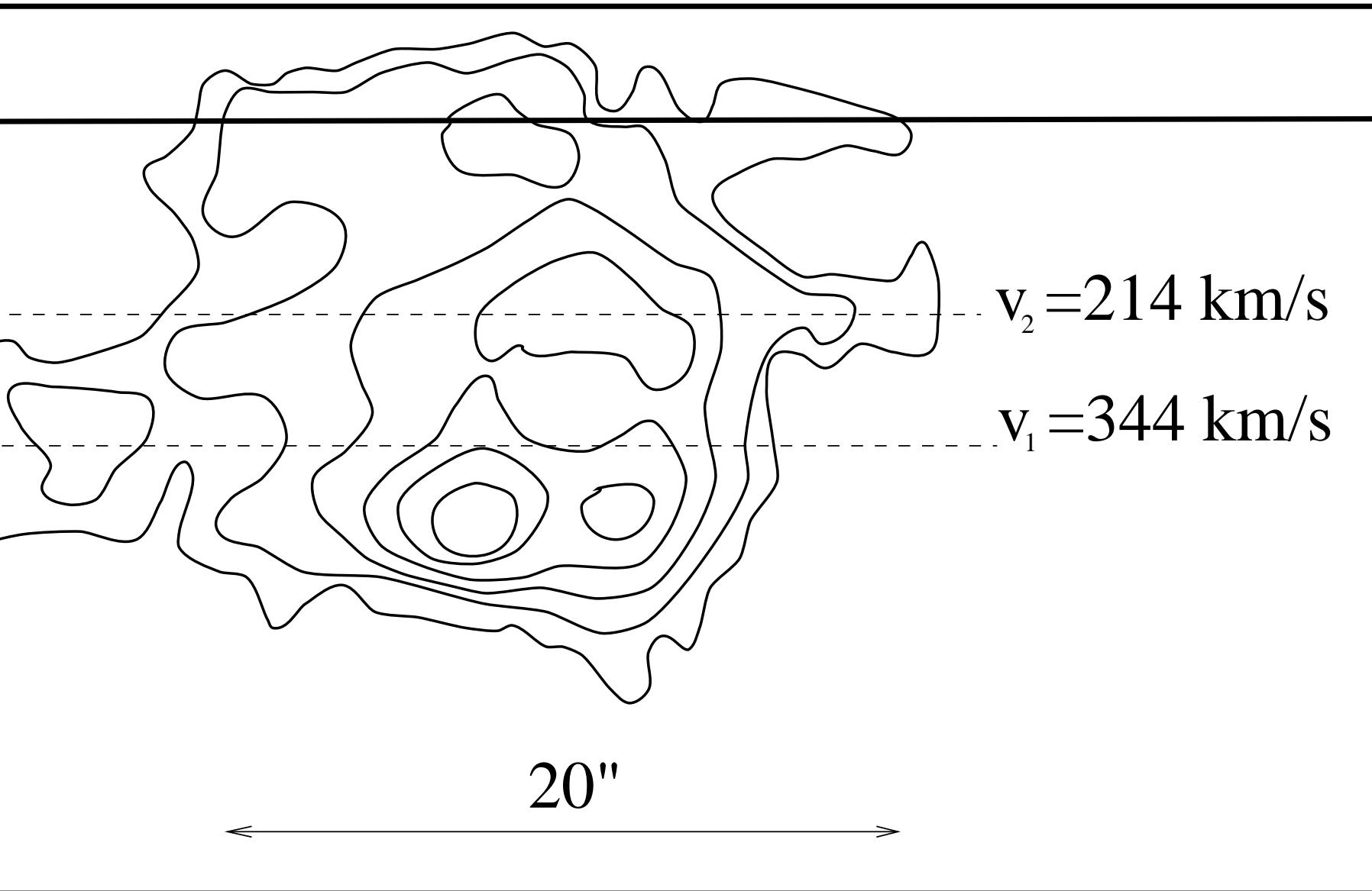
H $\alpha$



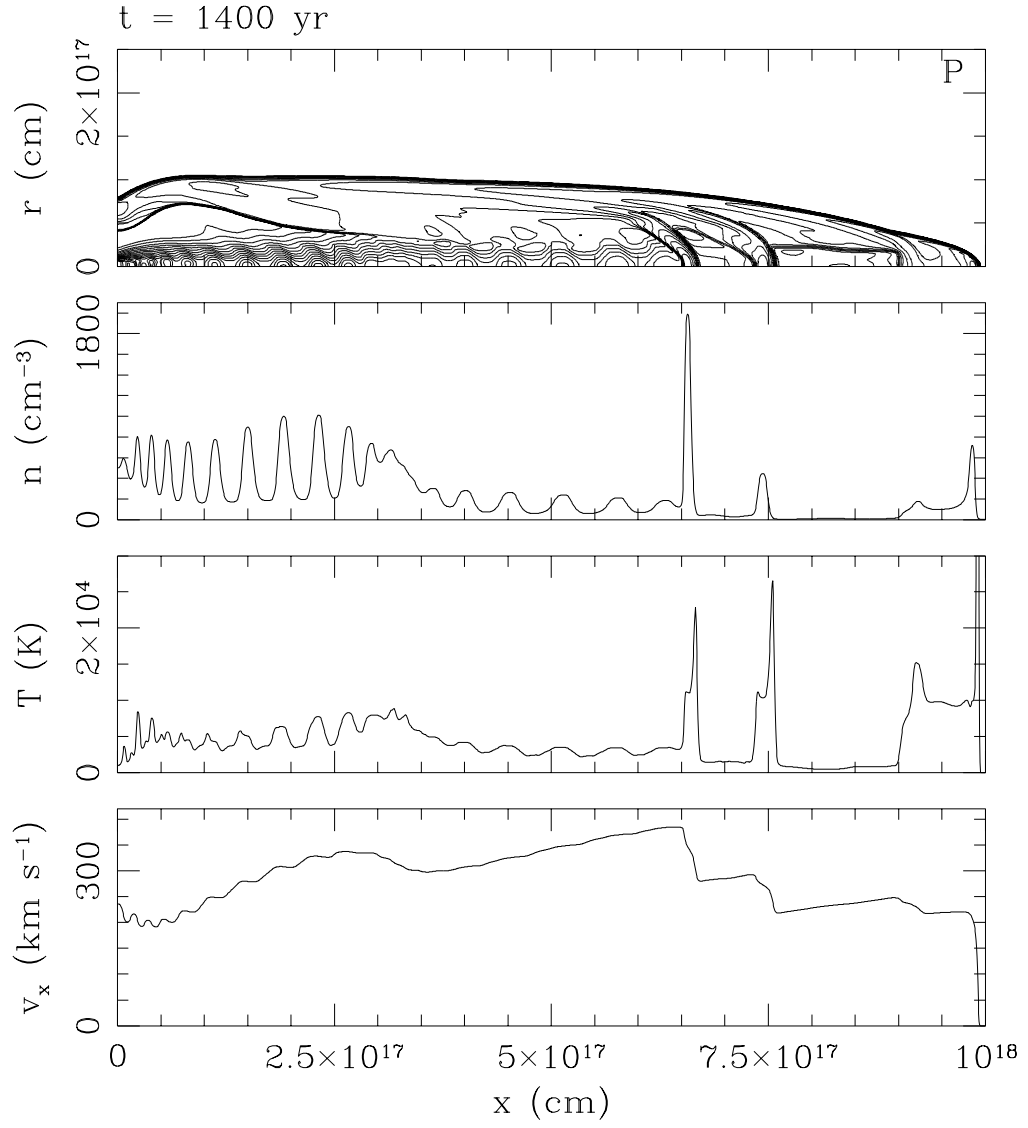
[S II] 6717+6731

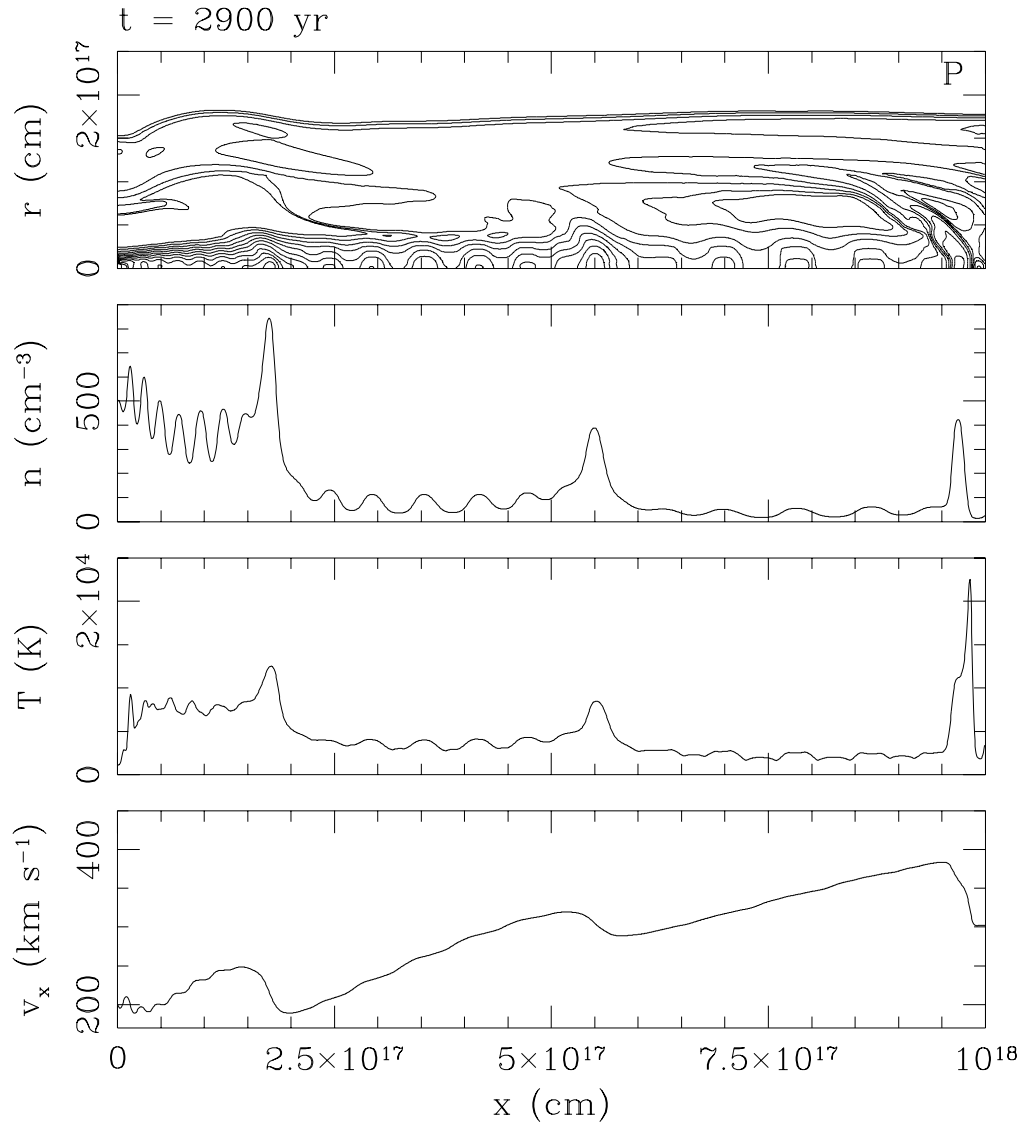




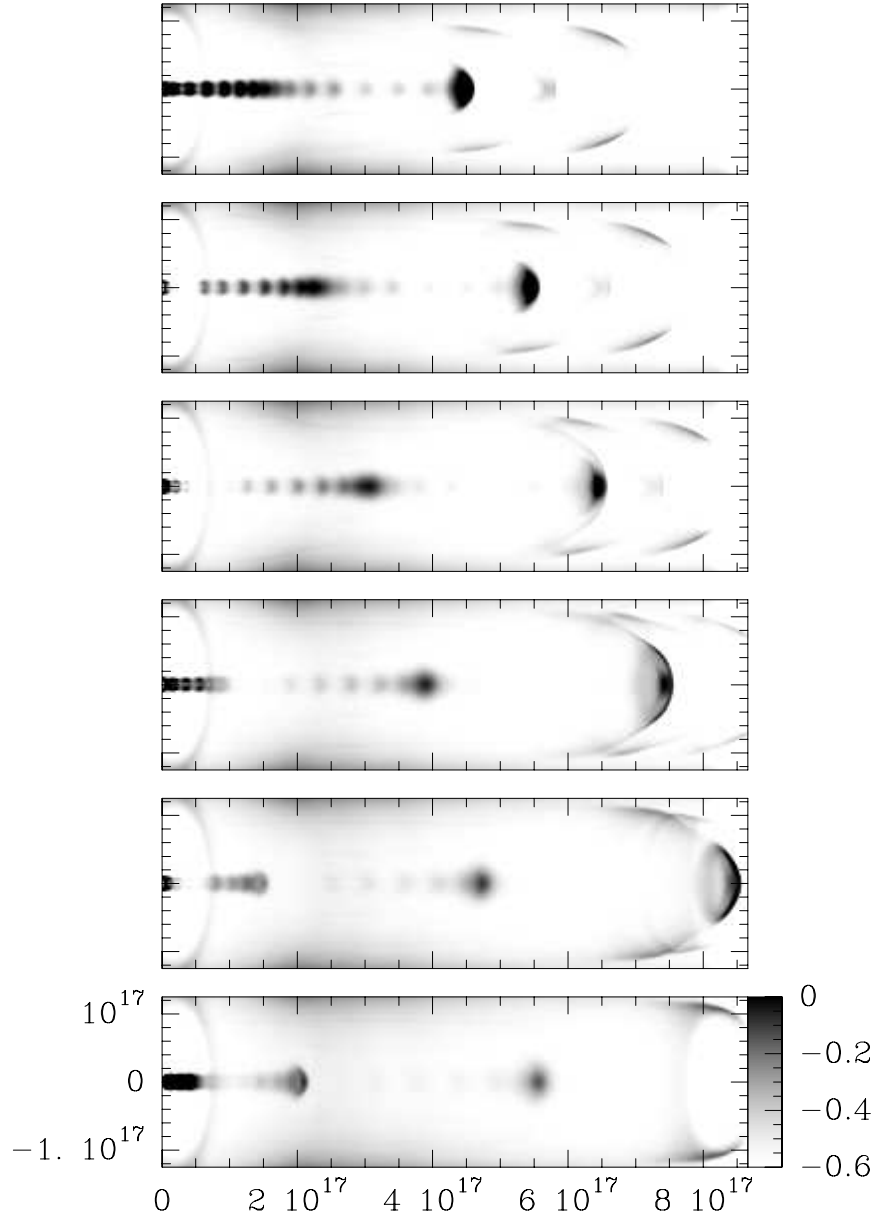




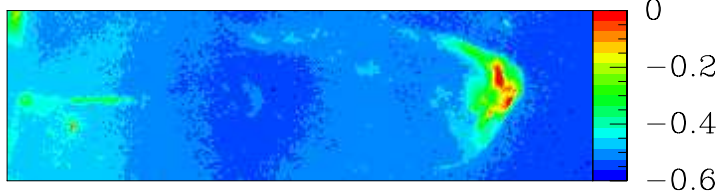
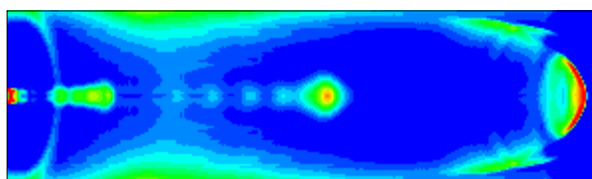




$t_0 = 2500 \text{ yr}$  ,  $\Delta t = 100 \text{ yr}$



H $\alpha$



[S II] 6717+6731

